

New tubulin binding site targeted by novel cyclodepsipeptide chemotype, gatorbulin-1

Susan Matthew^{1,7}, Qi-Yin Chen^{1,7}, Ranjala Ratnayake^{1,7}, Charles S. Fermain², Daniel Lucena-Agell³,
Francesca Bonato³, Andrea E. Prota⁴, Seok Ting Lim⁵, Xiaomeng Wang⁵, J. Fernando Díaz³, April L.
Risinger², Valerie J. Paul⁶, Maria Ángela Oliva^{3*}, Hendrik Luesch^{1,5*}

¹Department of Medicinal Chemistry and Center for Natural Products, Drug Discovery and
Development (CNPDP), 1345 Center Drive, Gainesville, Florida 32610, USA

²Department of Pharmacology, The University of Texas Health Science Center at San Antonio, 7703
Floyd Curl Drive, San Antonio, Texas 78229, USA

³Centro de Investigaciones Biológicas Margarita Salas, Consejo Superior de Investigaciones Científicas,
Ramiro de Maeztu 9, 28040 Madrid, Spain

⁴Laboratory of Biomolecular Research, Division of Biology and Chemistry, Paul Scherrer Institut, CH-
5232 Villigen, Switzerland

⁵Lee Kong Chian School of Medicine, Nanyang Technological University, 59 Nanyang Drive, 636921,
Singapore

⁶Smithsonian Marine Station, 701 Seaway Drive, Fort Pierce, Florida 34949, USA

⁷These authors contributed equally.

*email: luesch@cop.ufl.edu; marian@cib.csic.es

21 Tubulin-targeted chemotherapy has proven to be a successful and wide spectrum strategy against solid
22 and liquid malignancies. Therefore, new ways to modulate this essential protein could lead to new
23 antitumoral pharmacological approaches. Currently known tubulin agents bind to six distinct sites at
24 α/β -tubulin either promoting microtubule stabilization or depolymerization. We have discovered a new
25 binding site at the tubulin intradimer interface where a novel microtubule-destabilizing
26 cyclodepsipeptide, termed gatorbulin-1 (GB1) binds. GB1 has a unique chemotype and was isolated
27 from a marine cyanobacterium. We have elucidated this dual, chemical and mechanistic, novelty
28 through multidimensional characterization, including compound isolation, multi-nuclei NMR-based
29 structure determination, revealing the modified pentapeptide with a functionally-critical hydroxamate
30 group, and validation by total synthesis. We have investigated the pharmacology using isogenic cancer
31 cell screening, cellular profiling, and complementary phenotypic assays, and unveiled the underlying
32 molecular mechanism by *in vitro* biochemical studies and high-resolution structural determination of the
33 α/β -tubulin-GB1 complex.

34

35 Microtubules are polarized polymers consisting of α/β -tubulin heterodimers involved in cellular
36 structure, motility, proliferation, and intracellular trafficking¹. Pharmacological targeting of tubulin
37 dynamics at different sites (**Fig. 1a**) has been a validated target for cancer therapy for decades and has
38 mostly been linked to the antimitotic effects of these compounds, although increasing evidence has
39 emerged for the importance of non-mitotic effects¹. Natural products targeting tubulin in particular have
40 yielded a wealth of chemically diverse agents and provided the basis for several FDA-approved drugs,
41 both for cancer and other pathologies, and either alone or as ADC, including paclitaxel, vincristine,
42 maytansine, eribulin, and colchicine (**Fig. 1b,c**). Compounds can be classified based on their binding to
43 one of the six known binding sites, and even though they are all targeting tubulin, they have shown
44 distinct pharmacological effects. Therefore, there is a persistent interest in the identification of novel
45 microtubule-targeting agents. Two α/β -tubulin binding sites are associated with microtubule stabilization
46 (taxane and laulimalide/peloruside sites, **Fig. 1a,b**), while binding to four other sites causes microtubule
47 destabilization (vinca, maytansine, colchicine, and pironetin sites, **Fig. 1a,c**)¹.

48 Our investigation of marine cyanobacteria as a source of potential anticancer agents has previously
49 yielded the modified peptides dolastatins 10 and 15²⁻⁴, targeting the “peptide site” within the vinca
50 domain^{5,6}. Three antibody-drug conjugates (ADCs) with a dolastatin 10 analogue (monomethyl
51 auristatin E, MMAE) as the cytotoxic payload are approved for the treatment of various lymphomas and
52 refractory bladder cancer, while dolastatin 15-based ADCs have advanced to clinical trials⁴. We
53 identified both dolastatins 10 and 15 as indirect hypoxia-inducible factor (HIF) inhibitors based on
54 differential cytotoxicity against a panel of isogenic HCT116 colorectal cancer cells^{4,7}, which indicated
55 that HIF inhibition is functionally relevant for the mechanisms of action of these compounds. HIF is
56 activated in solid tumors, promotes metastasis, and targeted screening early in the drug discovery
57 process could provide a rapid indication for requisite selectivity for cancer treatment⁸⁻¹⁰. Using the same
58 isogenic screening system, we now identified a new antiproliferative agent that also possessed

preferential activity for oncogenic KRAS- and HIF-1 α -containing HCT116 cells and is a microtubule-destabilizing cyclodepsipeptide. We named the compound gatorbulin-1 (GB1, **1**, **Fig. 1c**), in analogy to eribulin (Eisai Research Institute), to symbolically represent the discovery of its unique chemical structure and pharmacological potential at the University of Florida and global Gator Nation partners. Here we report the bioassay-guided isolation, structure determination, synthesis, preliminary structure-activity-relationships, mechanism of action, target identification, and binding mode elucidation. Our studies revealed that GB1 represents a new chemical scaffold targeting a novel binding site near the colchicine site and displays distinct pharmacology (**Fig. 1a**).

Results

Isolation and structure determination of gatorbulin-1. Various collections of the cyanobacterium *Lyngbya cf. confervoides* during blooms off the coast near Ft. Lauderdale¹¹ (Broward County) were extracted with EtOAc–MeOH (1:1). The extract, previously proven to be rich in secondary metabolites and possessing antifeedant activity^{12,13}, was defatted with hexanes and the residue partitioned between *n*-BuOH and H₂O. The concentrated *n*-BuOH layer was applied onto diaion HP-20 column and fractions subjected to reversed-phase HPLC to afford GB1 (**1a**) as an optically active, colorless amorphous solid ($[\alpha]_D^{20}$ –84.0 (*c* 0.10, MeOH)) and as the most antiproliferative extract component by bioassay-guided isolation using colon cancer cells, along with a minor analogue, gatorbulin-2 (**1b**, **Fig 2a**). Doubling of virtually every signal in the ¹H NMR spectrum of **1a** recorded in DMF-*d*₇ suggested the presence of an asymmetric dimer or the presence of conformers in a ratio of 1:1. This observation coupled with the [M + H]⁺ ion peak at *m/z* 484.2043 obtained by HRESI/APCIMS and ¹³C NMR data suggested a molecular formula of C₂₀H₂₉N₅O₉ (calcd for C₂₀H₃₀N₅O₉, 484.2044) and consequently the presence of conformers in the NMR solvent. NMR analysis using ¹H NMR, ¹³C NMR, COSY, HMQC, and ¹H–¹³C HMBC data

82 was carried out for both conformers, revealing two sets of five spin-coupled systems as part of a
 83 pentapeptide structure; one signal set appeared slightly broader (**Table 1, Fig. 2b**).
 84 For both signal sets, one putative NH singlet each (δ_{H} 8.28 and 8.60) showed COSY correlations to sp^2 -
 85 methylene protons (δ_{H} 6.46/5.22 for conformer 1, 6.22/5.11 for conformer 2), which also appeared as
 86 singlets in the ^1H NMR spectrum. Correlations from the NH to the corresponding olefinic methylene
 87 carbon (δ_{C} 101.8 and 103.0), to a quaternary sp^2 hybridized carbon (δ_{C} 136.3 and 136.2) and to two
 88 carbonyl carbons (δ_{C} 165.9/170.5 for conformer 1 and 166.8/170.2 for conformer 2) defined the first unit
 89 as a dehydro-alanine (DhAla) residue (**Table 1**).
 90 Two singlets of another signal set for heteroatom-bound protons (δ_{H} 7.26/7.09 for conformer 1 and δ_{H}
 91 7.39/7.21 for conformer 2) showed cross-peaks in the COSY spectrum, suggesting a primary amide.
 92 Another set of singlets at δ_{H} 3.09 and 3.14 was indicative of an *N*-methyl tertiary amide group;
 93 expectedly these signals exhibited HMBC correlations with a carbonyl carbon of the adjacent residue
 94 (δ_{C} 169.9 and 169.7) and for conformer 1 also to the α -carbon of the *N*-methylated amino acid (δ_{C} 58.0).
 95 Rigorous 2D NMR analysis established the second unit as an *N*(α)-methyl- β -hydroxy-asparagine (*N*(α)-
 96 Me- β -OH-Asn). Even though the significant broadening of all signals for this unit for the second
 97 conformer resulted in fewer HMBC correlations, all ^1H and ^{13}C NMR resonances could be assigned
 98 except for the α -carbon since its NMR signal was too broad to be observed (**Table 1**).
 99 The third multi-proton spin system consisted of two methylenes (δ_{H} 4.31/3.25, 2.58/1.58 for conformer
 100 1), two methines (δ_{H} 4.42, 2.53) and one methyl group (δ_{H} 1.12 d). COSY analysis established their
 101 arrangement supported by HMBC data. The terminal methine and methylene carbons of this spin system
 102 appeared to be nitrogenated (δ_{C} 62.6, 56.9) and the HMBC correlation of one of the methylene protons
 103 (δ_{H} 4.31) to one of the methine carbons (δ_{C} 62.6) clarified that the carbons were joined in a 3-methyl
 104 pyrrolidine structure, which upon further analysis of HMBC correlations to a carbonyl carbon (δ_{H} 170.8)

105 identified the third residue as a 4-methylproline unit (4-MePro). In a similar fashion, a signal set
106 corresponding to the second conformer for this unit was unambiguously identified (**Table 1**).

107 Analysis of the fourth spin system was straightforward and this unit consisted of only one methine and a
108 methyl group and NMR data, consistent with an acylated lactic acid (Lac) moiety. The last unit
109 exhibited similarity to a lactic acid or alanine moiety, yet the α -carbon resonated at higher field than the
110 corresponding carbon for lactic acid (δ_C 64.7 and 60.0) and thus more likely bore a nitrogen atom, which
111 then in turn had to bear a substituent that was not accounted for yet. This NMR analysis so far led to the
112 assignment of all atoms except one oxygen and hydrogen based on HRMS analysis. In the 1H NMR
113 spectrum, the only unassigned signal at this point was a signal for an exchangeable proton at δ_H 11.35
114 (br s) for conformer 1 and at δ_H 10.58 (br) putatively for conformer 2, which could not be rationalized
115 by a secondary amide since it did not show a COSY correlation to the nitrogen-bearing methine while
116 also resonating too far downfield. The chemical shifts were consistent with carboxylic acid protons
117 which could exist in a linear structure; however, it would not leave a substituent for the nitrogen atom in
118 the alanine-like moiety. Therefore, a bond between two heteroatoms, nitrogen and oxygen, had to be
119 invoked which led us to propose a *N*-hydroxy group in a cyclic hydroxamate (*N*-OH-Ala); its hydroxy
120 proton was also expected to resonate between δ_H 10–12 as observed.

121 The doubling and overlap of signals for several carbonyl carbons for different conformers slightly
122 complicated the sequencing of the individual units. To ultimately prove the existence of the
123 hydroxamate and to validate the nature of the nitrogen atoms we carried out a 1H – ^{15}N HMBC analysis
124 (**Table 1**). Correlations of the H-3a/b methylene protons of the DhAla unit to a nitrogen atom resonating
125 at δ_N –258.2 (relative to external $MeNO_2$, δ_N 0.0) supported the earlier assignment of a secondary amide
126 (**Fig. 2b,c**). The *N*-Me protons of the *N*-Me-3-OH-Asn showed HMBC correlations to a nitrogen
127 possessing a chemical shift of δ_N –273.8, an expected value for a tertiary amide (**Fig. 2b,c**). Most
128 importantly and confirmatory for the hydroxamate moiety were two- and three-bond correlations from

the α -methine and the β -methyl protons to a signal at δ_N -202.6 (**Fig. 2b,c**) which is in agreement with literature values for hydroxamate nitrogens (δ_N -199.2 for polyoxypeptin A¹⁴), further validating the proposed structure for GB1 (**1a**). The ^1H - ^{15}N HSQC spectrum, in addition to the secondary amide proton for DhAla (δ_N -258.2), also showed one-bond correlations for both protons of the primary amide functionality for both conformers (δ_N -280.5 and -279.6, **Fig. 2c**). The presence of the hydroxamate functionality was supported analytically by ferric hydroxamate complex formation¹⁵.

Further support for the proposed structure was found with the isolation of its *N*-deoxy-derivative, termed gatorbulin-2 (GB2), or *N*-deoxy-GB1 (**1b**, **Fig. 2a**). The ^1H NMR spectrum was strikingly similar to the one of **1a**, including the presence of conformers in a 1:1 ratio in DMF-*d*₇ (Supporting Information, **Table S1**). The most significant difference appeared to be the lack of the N-OH protons at δ_H 10–12; instead a new set of doublets appeared in the range for amide protons (δ_H 8.21 and 8.38 for conformers 1 and 2).

To establish the absolute configuration, we performed acid hydrolysis to liberate the individual units and synthesized all isomers of the amino acid standards for comparative chiral HPLC analysis and advanced Marfey's analysis. The 4-MePro standards were prepared as described previously¹⁶ and the *N*(α)-Me- β -OH-aspartic acid stereoisomers as described in the Supporting Information. We detected *L*-erythro-*N*(α)-Me- β -OH-Asp, (2*S*,4*S*)-4-Me-Pro, and L-Lac in the hydrolyzate of **1a**. The structures and identical absolute configurations were confirmed by conversion of **1a** into **1b** via TiCl₃-mediated reduction (**Fig. 2a**)¹⁷. Upon acid hydrolysis, **1b** yielded L-Ala as detected by chiral HPLC analysis, establishing the remaining stereogenic center.

Structure validation by the total synthesis of gatorbulin-1. To prove the structure and overcome the supply issue, we embarked on the total synthesis. The retrosynthetic analysis of total synthesis of GB1

(**1a**) is shown in **Figure 2d**. The final product **1a** could be obtained from the fully masked cyclized precursor **2** by sequential deprotection. The site between 4-MePro and (Se)-phenylselenocysteine (Sec(Ph)) was chosen for macrolactamization. In linear precursor **3**, Fmoc-Fm pair was designed as the protection groups of amino and carboxy termini, respectively, which could be cleaved simultaneously with base to provide the precursor of macrocyclization¹⁸. Sec(Ph) was proposed as the pro-unit of DhAla¹⁹. Linear compound **3** was disconnected into four building blocks **4–7**, which could be constructed from commercially available reagents (e.g., **6** from **8** and **9**) using established or modified protocols.

Figure 2e depicts the synthetic route to GB1 (**1a**). The synthesis of acid **4** was adopted from published procedures²⁰. (2*R*,3*R*)-epoxysuccinic acid (**10**) was converted to *erythro*-*N*(α)-methyl-3-hydroxy-L-aspartic acid (**11**) by treatment with methylamine-water under reflux. Then **11** was selectively esterified with acidic methanol under refluxing²¹ to provide monoester **12**. Without purification, aminolysis of **12** with ammonia (gas) in MeOH provided *N*(α)-methyl- β -hydroxy-asparagine (**13**)^{20,21}, which had poor solubility in MeOH, so that pure product could be obtained by simple filtration. Sequential protections of the groups of **13** using standard methods²² provided full masked compound **17**. Finally, acid **4** was obtained from **17** by hydrogenation with palladium catalyst.

The synthesis of building block of allyloxamine **5** adopted the triflate method²³. Allyl was chosen as NOH protecting group as it could be selectively removed by Pd(Ph₃P)₄ in the presence of dehydropeptide. Acid **6** was synthesized from (4*S*)-*N*-Boc-4-methyl-Pro (**9**) and benzyl-L-lactate (**8**) by standard protocols of esterification, protection and deprotection. Following established procedures¹⁹, *N*-Boc-serine (**22**) was converted to BocSec(Ph) (**24**) via β -lactone **23**, which was esterified with FmOH to provide building block **7**. Dehydroalanine could be obtained from phenylselenocysteine by oxidative β -elimination. The fusion of building blocks was initiated by coupling of acid **4** with allyloxamine **5**. Acid **4** was activated to the acid chloride, which was then coupled with **5** in presence of AgCN^{24,25} to provide

176 **25** in 50% yield. This acylation was not successful when other common coupling reagents were used
177 because of poor nucleophilicity of the nitrogen and high steric hindrance²⁶. Compound **26** was obtained
178 in 78% yield by BEP-mediated coupling²⁷ of acid **6** with the free methyl amine generated by selective
179 deprotection of **25**. Selective removal of *t*-butyl group of **26** by TMSOTf/2,6-lutidine²⁸ afforded acid **27**,
180 which was coupled with free amine from **7** using BOP as coupling reagent to yield the linear compound
181 **3** in 86% yield. The use of the *t*-butyl protecting group prevented diketopiperazine²⁹ formation upon
182 coupling of **6** and **25**, and ensured that trityl and TBS groups were intact for the generation of acid **27**.
183 Both Fmoc and Fm protection groups were removed simultaneously when compound **3** was exposed to
184 Et₂NH in MeCN. The macrocyclization was mediated by PyBOP/HOAt to give macrocycle **2** in 60%
185 yield for two steps. Removal of TBS of **2** with the TBAF/HOAc buffer^{22,30} provided **28**, and subsequent
186 oxidation of SePh with NaIO₄¹⁹ yielded dehydropeptide **29**. Trityl was removed with TFA in CH₂Cl₂³¹ to
187 yield primary amide **30**. The removal of allyl group by Pd(PPh₃)₄/PhSiH₃^{30,32} provided final product **1a**.
188 The removal sequence for trityl and allyl groups are interchangeable; however, the yield would drop
189 from 66% to 35%. GB1 (**1a**) was purified by reverse TLC plate (C18). The synthetic sample was
190 identical to the isolated natural product, which was verified by NMR, HRMS and optical rotation
191 (Supporting Information).

193 **Gatorbulin-1 cellular profiling identifies the mechanism of action.** GB1 (**1a**) was identified as the
194 extract's active component against colon cancer cells and showed an IC₅₀ of 0.80 μM against HCT116
195 colorectal cancer cells (**Fig. 3a**), while **1b** was inactive at the highest concentration tested (IC₅₀ > 10
196 μM, not shown), indicating that the hydroxamate moiety is indispensable to the antiproliferative activity.
197 Isogenic cell line selectivity screening indicated preferential activity against parental HCT116 compared
198 with the oncogenic KRAS knockout or double knockout of both HIF-1α and HIF-2α transcription
199 factors (**Fig. 3a**)⁷. Deconvolution using single knockouts of HIF-1α and HIF-2α clearly demonstrated

that only cells depleted in HIF-1 α had reduced susceptibility to GB1, which is consistent with HIF-1 α being in the same pathway and activated by oncogenic KRAS. Furthermore, normal epithelial colon cells (CCD841-CoN) were less inhibited, indicating an additional promising level of selectivity (**Fig. 3a**). The preference for HIF-1 α expressing cells parallels the selectivity profiles for microtubule agents we previously discovered (dolastatins 10 and 15)^{4,7}. DNA content analysis revealed the concentration-dependent G2/M cell cycle accumulation characteristic for antimitotic agents (**Fig. 3b**). A concentration of GB1 (4 x IC₅₀) that results in a complete antiproliferative response, initiated a concomitant downregulation of the HIF-1 α target gene *VEGFA* in parental HCT116 cells (**Fig. 3c**) that was even more pronounced than for dolastatin 15⁴, which also elevated GB1's potential as antiangiogenic agent. Consistent with the role of microtubule dynamics in angiogenesis³³, GB1 also inhibited endothelial tube formation without cytotoxicity (**Fig. 3d-f**). Endothelial cell tube formation in Matrigel mimics the process of blood vessel formation *in vivo*.³³ Our study suggested that 10 μ M GB1 was necessary to block the ability of human umbilical vein endothelial cells (HUVECs) to form tube-like structures within 3 h (**Fig. 3d**). Quantification of the structural network revealed a significant reduction in the number of nodes, number of junctions, number of meshes and total length of tubes (**Fig. 3e**). Importantly, GB1 did not affect HUVEC cell viability, even after 24 h (**Fig. 3f**). Taken together, this reveals an antiangiogenic potential of the compound in inhibiting the formation and stabilization of a three-dimensional vascular network. The additional *VEGF* downregulation in growth factor secreting cells, which is a driver of angiogenesis, is expected to result in a pronounced antiangiogenic action of GB1 *in vivo*.

The NCI-60 cell line screen data (**Fig. 3g**), analyzed by the COMPARE algorithm³⁴, were indicative of a cytotoxicity profile most related to antimitotic/tubulin agents, including paclitaxel, eribulin, colchicine and vinca bis-indole alkaloid derivatives (*P* 0.75–0.85), suggesting that the biochemical mechanisms of action are related. While GB1 displayed an IC₅₀ > 10 μ M against normal mucosal colon cells, it had

submicromolar activity against HCT116 cells (GI_{50} 306 nM) and was even more potent against COLO205 cells (GI_{50} 92 nM) based on the NCI-60 data. Other susceptible cell types included certain melanoma (SK-MEL-5), ovarian (OVCAR-3) and prostate (DU-145) cancer cells, which corresponds to the certain cancers where microtubule agents have been successful. Additionally, cervical and breast cancers are relevant indications, prompting additional studies in these cell types (see below)³⁵.

229

Target identification and gatorbulin-1 underlying molecular mechanism. First, using a biochemical assay, we demonstrated that GB1 directly inhibits tubulin polymerization *in vitro* (**Fig. 4a,b**). Second, we tested GB1 binding to commonly targeted sites for microtubule-destabilizing agent including the vinblastine, maytansine and colchicine sites (**Fig. 1a**), by employing fluorescent bona fide probes³⁶⁻³⁸. GB1 was unable to displace the fluorescent derivatives of eribulin and maytansine indicating that it did not bind to these sites. However, GB1 successfully competed with a fluorescent probe of the colchicine site (MTC) (**Fig. 4c,d**) with an apparent binding affinity of $1.01 \pm 0.08 \times 10^6 \text{ M}^{-1}$, which is below colchicine apparent binding affinity ($1.5 \times 10^7 \text{ M}^{-1}$;³⁹).

We performed subsequent cell-based studies with GB1 in comparison with combretastatin A4 (CA-4), a known colchicine site binder. We demonstrated that GB1 promotes microtubule depolymerization in A-10 (rat smooth muscle) interphase cells, similar to CA-4, although with lower potency (**Fig. 4e**). GB1 promoted aberrant mitotic spindle formation at submicromolar concentrations (**Fig. 4f**). HeLa cervical cancer cells were highly susceptible to GB1; the compound induced accumulation of cells in the G2/M cell cycle phases (**Fig. 4g**). We then compared the antiproliferative effects of GB1 and CA-4 in a panel of triple negative breast cancer (TNBC) cells and in drug resistant models, including parental and Pgp-overexpressing SK-OV-3 ovarian adenocarcinoma cells and parental and β III expressing HeLa cells⁴⁰. The compounds showed a different fingerprint. GB1 does not circumvent Pgp or β III-tubulin mediated drug resistance (**Fig. 4h**), indicating that it was mechanistically distinct from CA-4. Additionally, it has

a distinct profile of relative efficacy against a panel of TNBC cell lines as compared to CA-4 (48 h, **Fig. 4h,i**). MDA-MB-231 cells pre-treated with GB1 for 24 h demonstrated a significant concentration-dependent inhibition of cancer cell migration and invasion abilities across a transwell membrane as compared to DMSO-treated controls, without significantly affecting cell viability (**Fig. 4j**). This phenotype is also consistent with the microtubule-targeting mechanism⁴¹. Taken together, the mechanistic biochemical and pharmacological data suggested that GB1 can block ligand binding to the colchicine site but may not fit in the classic pocket, resulting in a distinct profile of cellular activity.

To further probe our hypothesis and identify the specific binding mechanism, we aimed at high-resolution macromolecular crystallography. T₂R-TTL system (two α/β -tubulin dimers in complex with the stathmin-like protein RB3 and tubulin tyrosine ligase) has successfully produced several structures of ligand bound to tubulin using X-ray crystallography⁴². However, GB1 soaking experiments did not reveal any difference density related to the ligand. We finally succeeded using the T₁-DARPin (T1D) complex that was previously used to solve the structure of colchicine-bound tubulin by Serial Millisecond Crystallography⁴³. We solved the structure of T1D-GB1 at 1.94 Å resolution (**Table S2**), and we unequivocally found ligand density at a new site that is close but clearly different from the colchicine binding site (**Fig. 5a**). This binding site sits at the intra-dimer interface between α - and β -tubulins. It is equivalent to the vinca site but the defined pocket boundaries are reversed (**Fig. 5b**), meaning that contacts with loop T7, helix H10 and strand S9 are provided by β -tubulin (whereas these are α -tubulin in the vinca site) and α -tubulin supplies interactions by loops T5 and H6-H7 (which correspond to β -tubulin in the vinca site).

The structure superimposes very well with the T1D apo-structure (PDB 4drx) with an overall r.m.s.d. of 0.39 Å over 771 C α -atoms, suggesting that the binding of GB1 does not affect the conformation of tubulin. Indeed, there are no major changes on the secondary structural elements surrounding the compound. GB1 is a cyclic peptide that shares a slightly greater buried interface area with α -tubulin

272 (304 Å²) than with β-tubulin (278 Å²) displaying interactions with both tubulin molecules. GB1 methyl-
 273 proline group (4-MePro) is sandwiched at the bottom of the pocket within the α-tubulin molecule
 274 between αY210 (helix H6) and αY224 (helix H7) (**Fig. 5c**), while the carbonyl moiety of this residue
 275 points toward the lateral chain of βQ247 (loop T7). The next clockwise residue is the dehydro-alanine
 276 (DhAla) that interacts with α-tubulin through hydrogen bond to the αR221 (loop H6-H7) side chain
 277 amide. The same carbonyl additionally co-coordinates a crystallographic water molecule that is shared
 278 with other carbonyl and hydroxy groups of the compound. The following residue is an alanine that
 279 interacts with β-tubulin through a coordinated crystallographic water molecule to the βV355 (strand S9)
 280 amide nitrogen. The hydroxamate of this alanine (*N*-OH-Ala) hydrogen bonds to βD329 (helix H10)
 281 side chain Oδ2 and Oδ1 (**Fig. 5c**), rationalizing the critical function of the hydroxamate for binding. The
 282 hydroxy propanamide residue (*N*(α)-Me-β-OH-Asn) makes extensive contacts with α- and β-tubulins
 283 through loop T5, including the carbonyl moiety of αP175 and αQ176 and the carbonyl and the amide of
 284 αS178, and strand S9, with βK352 main chain and βV353 amide nitrogen (**Fig. 5d**). Additionally, the N-
 285 Me group of this residue further hydrogen bonds to βV353 carbonyl moiety. The carbonyl of the lactic
 286 acid (Lac) that closes the ring with 4-MePro further stabilizes contacts with the α-tubulin loop T5
 287 through hydrogen bond to the carbonyl of αQ176.

288 The tubulin-colchicine (PDB 5nm5) and tubulin-GB1 structures superimpose with an overall r.m.s.d of
 289 0.497 Å over 756 C_α-atoms with the main differences located at β-tubulin loop T7 and α-tubulin loop T5
 290 (**Fig. 5e**). These loops imperatively change their conformations upon colchicine binding because,
 291 otherwise, the trimethoxy phenyl ring of colchicine (**Fig. 1a**) would clash with βL247 and βN248 (loop
 292 T7) and the amide of ring B would clash with the αT179 (loop T5). The presence of GB1 at the new site
 293 precludes the simultaneous binding of a second ligand in the colchicine binding site due to GB1
 294 interactions with those loops, which correlates with the results of our competition assays that increasing
 295 concentrations of GB1 prevents the MTC fluorescence probe binding to tubulin (**Fig. 4c,d**).

296

297 **Discussion**

298 We took an integrated approach towards natural products drug discovery by targeting minor, highly
299 bioactive compounds from a chemically prolific cyanobacterium, combining innovative screening and
300 rigorous bioassay-guided isolation and structure determination with chemical synthesis to overcome the
301 supply problem, and achieving in depth-mechanistic studies as well as direct target and binding site
302 identification. We advocated for such an approach to fully exploit the proven potential of natural
303 products and increase the value of bioactive natural products⁴⁴. The ultimate key for a successful natural
304 product drug discovery campaign is the choice of the source organism. We have been focusing on
305 marine cyanobacteria, which are prolific yet underexplored marine prokaryotes with a tremendous
306 biosynthetic potential. The gatorbulin-yielding sample was derived from a blooming “superproducer” of
307 secondary (specialized) metabolites (natural products) that previously yielded lyngbyastatins 4-6,
308 pompanopeptins A and B, tiglicamides, largamides/largamide D oxazolidinone, most of which are
309 noncytotoxic serine protease inhibitors^{12,13,45-47}. Beyond showcasing the biosynthetic capacity of marine
310 cyanobacteria, our discovery of GB1 exemplifies that marine cyanobacterial natural products occupy
311 therapeutically relevant chemical space that could lead to the discovery of new biology, chemical tools
312 or even drug leads.

313 GB1 is a small (MW < 500 g/mol) cyclodepsipeptide, unique from most cyanobacterial modified
314 peptides or peptide-polyketide hybrids, which dominate the landscape of bioactive natural products
315 produced by marine cyanobacteria⁴⁸. GB1 is densely functionalized with all amino acids being modified
316 and the presence of one hydroxy acid. Natural products possessing the three main unusual structural
317 features of GB1 (the hydroxamate, C-hydroxylated and dehydro-amino acids) have not been reported.
318 The 4-methylproline residue is also rare feature but has been previously found in cyanobacterial natural
319 products¹⁶. Interestingly, the hydroxamate group that is typical for metal chelators and present in other

320 antiproliferative compounds⁴⁹, plays a functional role in GB1's binding to β -tubulin as the major
321 mechanism of antiproliferative action, although the additional metal binding ability potentially increases
322 the pharmacological complexity of GB1.

323 Tubulin targeting agents strongly affect microtubule dynamics, which is a key feature for the
324 functioning of these filaments in a wide range of biological processes. In fact, many of these compounds
325 have been originally discovered within the extracts from living sources that often have mobility
326 restrictions and hence, use them as a protection mechanism against consumers. Some compounds
327 promote microtubule stabilization through the interaction with either the taxane site (in the lumen of the
328 microtubule) or the polo/lau site (wall of the microtubule). The underlying mechanism is under
329 discussion but these compounds prevent microtubule depolymerization by locking lateral and/or
330 longitudinal contacts. Microtubule-destabilizing compounds are more common and frequently more
331 toxic. These induce rapid microtubule disassembly and prevent tubulin polymerization by two different
332 molecular mechanisms: blockage^{50,51} and wedging^{52,53}. Compounds that bind to the tip (maytansine) site
333 (top surface of β -tubulin) or pironetin site (bottom surface of α -tubulin) prevent the incorporation of a
334 new tubulin heterodimer to the microtubule-growing end due to the inactivation of the contact surfaces.
335 Hence, these follow a blockage mechanism. Meanwhile, compounds interacting with the colchicine or
336 the vinca site block the essential curve-to-straight conformational change in tubulin upon assembly,
337 which necessarily comprise microtubule formation. Our GB1 high-resolution structure revealed a new
338 site and contributed to understanding the molecular mechanism underlying the compound's
339 destabilization effect. GB1 binds to a pocket localized between α - and β -tubulin, close to the colchicine
340 site and equivalent to the vinca site (that sits between two tubulin heterodimers), denoting a common
341 underlying mechanism to destabilize microtubule formation: wedging. The colchicine site is an
342 elongated pocket, where some compounds (colchicine, podophyllotoxin or noscapine) bind to the first
343 third, interacting with β -tubulin S9 and H7 (some also interact with the α -tubulin T5 loop), whereas

344 other compounds (e.g., nocodazole) bind deeper and also interact with the β -tubulin beta sheet of the N-
345 terminal domain^{52,54,55}. None have the extensive interactions with α -tubulin observed with GB1.

346 Most tubulin-targeting agents bind to β -tubulin, which is the active molecule within the heterodimer
347 upon GTP hydrolysis, with the exception of the pironetin site that is localized in α -tubulin. Tubulin has
348 been revealed as a complex molecule since it includes two similar targeting sites that comprise
349 interfaces of the two proteins either, within the heterodimer (intradimer interface, gatorbulin sites) or
350 between two heterodimers (interdimer interface, vinca site). Interestingly, these sites are equivalent but
351 contact surfaces are swapped between tubulin subunits. The top surface contains α -tubulin (vinca) or β -
352 tubulin (gatorbulin-1) residues, whereas the bottom surface contributes with β -tubulin (vinca) or α -
353 tubulin (gatorbulin-1) amino acids. Since tubulin is a key target for the treatment of cancer, this
354 increases our options for the screening and development of new, safer and more effective drugs. GB1 is
355 a cyclic depsipeptide that represents a new chemotype that differs from other peptides targeting tubulin
356 such as dolastatin 10 and, possesses low toxicity and molecular weight, adding to its promising small-
357 molecule, drug-like properties and translational potential.

358

359 **Acknowledgements**

360 This research was supported by the National Institutes of Health, NCI grants R01CA172310 (H.L.) and
361 R50CA211487 (R.R.) and NIGMS grant P41GM086210 (H.L. and V.J.P.), Commercialization Fund
362 Award from UF Innovate (University of Florida Office of Technology Licensing), and Debbie and
363 Sylvia DeSantis Chair professorship (H.L.) and the Greehey Endowment (S.L.M.). The biochemical and
364 the crystal structure work was supported by Ministerio de Ciencia e Innovación PID2019-104545RB-I00
365 and Fondo de Investigaciones Sanitarias COV20/01007 to J.F.D and H2020-MSCA-ITN-2019 860070
366 TUBINTRAIN (to J.F.D and A.E.P) and PIE 201920E111 from Consejo Superior de Investigaciones

367 Científicas (CSIC) to J.F.D. We thank Wesley Yoshida (University of Hawaii at Manoa) for assistance
368 with the ¹⁵N NMR experiments and Long H. Dang (UF Department of Medicine) for providing the
369 HCT116 knockout cells. We thank Susan L. Mooberry (UT Health Science Center at San Antonio) for
370 support with the pharmacological studies. We thank Ganadería Fernando Díaz for calf brains supply and
371 staff of beamline XALOC (ALBA, Cerdanyola del Vallès, Spain) for their support. We thank Cora
372 Petersen for her assistance with the cell proliferation studies.

373

374

375 **Author contributions**

376 **S.M.**, isolation, structure determination and preliminary bioactivity studies, data interpretation

377 **Q.Y.C.**, total synthesis, analytical compound characterization

378 **R.R.**, mechanistic studies, cellular profiling, cell cycle, COMPARE and gene expression analysis,
379 preliminary tubulin polymerization assays, data interpretation, final figure preparation

380 **C.S.F.**, immunofluorescence, cell cycle, tubulin polymerization assays, TNBC and drug resistant panel
381 profiling

382 **D.L.A.**, ligand displacement assays

383 **F.B.**, crystallization experiments, data collection

384 **A.E.P.**, assistance and troubleshooting with the production and expression of DarPin and the design of
385 the TD1-GA-1 crystallization system

386 **S.T.L.**, angiogenesis, migration and invasion assays

387 **X.W.**, supervision of angiogenesis, migration and invasion assays, data interpretation

388 **J.F.D.**, supervision of ligand displacement assays, data interpretation, manuscript editing

389 **A.L.R.**, supervision of immunofluorescence, HeLa cell cycle, tubulin polymerization assays, TNBC and
390 drug resistant panel profiling, data interpretation

391 **V.J.P.**, collection and identification of cyanobacterium, manuscript editing

392 **M.Á.O.**, supervision of crystallization, binding site analysis and data interpretation and discussion,
393 manuscript editing

394 **H.L.**, overall project supervision, study design and integration, data interpretation, manuscript
395 preparation

396

397 All authors have contributed to the writing of the manuscript.

398

399 **Competing Interest Statement**

400 UF has filed a patent application on the composition of matter, synthesis and methods of use.

401

402 **References**

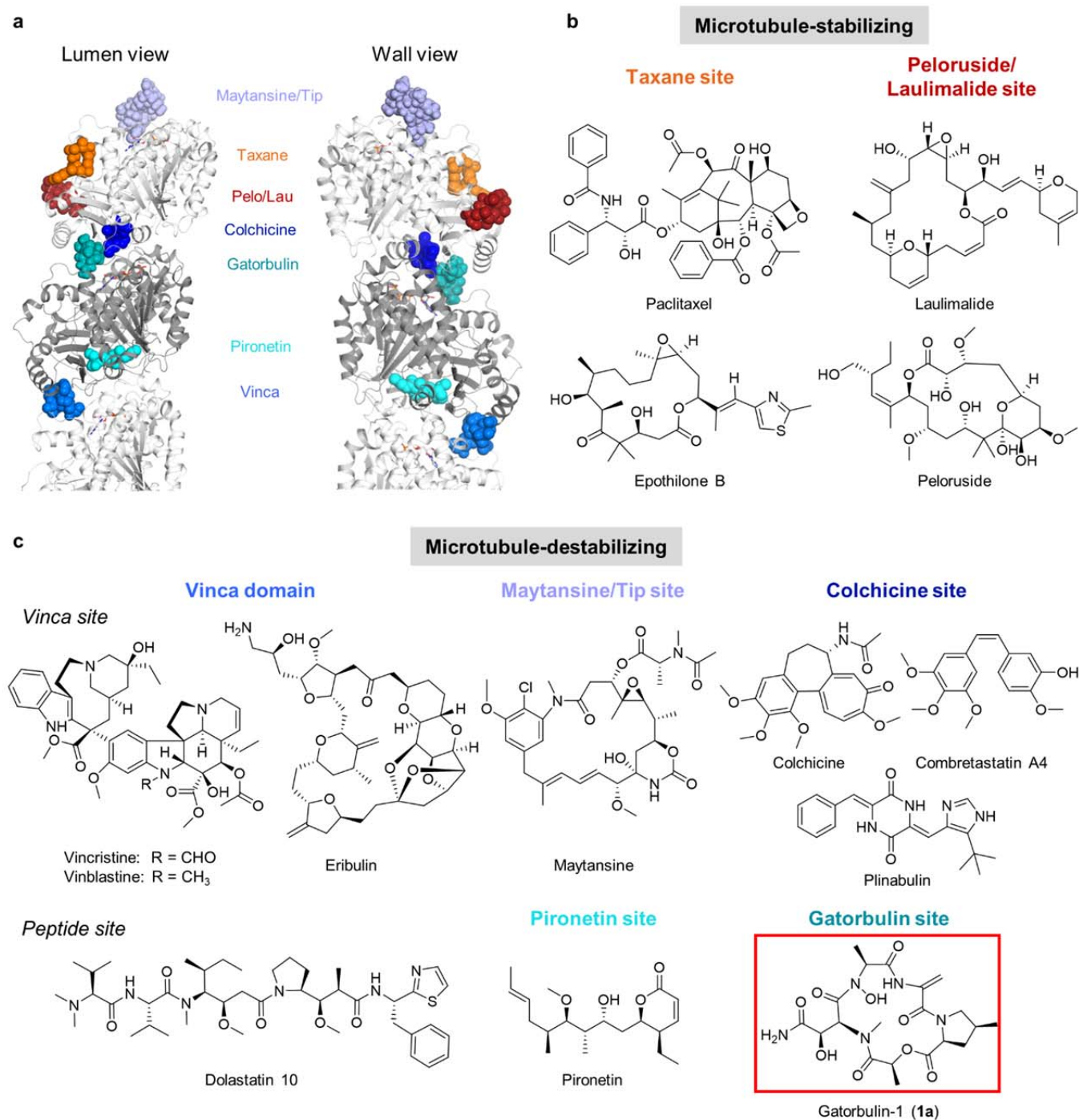
- 403 1. Risinger, A. L. & Du, L. Targeting and extending the eukaryotic druggable genome with natural
404 products: cytoskeletal targets of natural products. *Nat. Prod. Rep.* **37**, 634–652 (2020).
- 405 2. Luesch, H., Moore, R. E., Paul, V. J., Mooberry, S. L. & Corbett, T. H. Isolation of dolastatin 10
406 from the marine cyanobacterium *Symploca* species VP642 and total stereochemistry and
407 biological evaluation of its analogue symplostatin 1. *J. Nat. Prod.* **64**, 907–910 (2001).
- 408 3. Salvador-Reyes, L. A., Engene, N., Paul, V. J. & Luesch, H. Targeted natural products discovery
409 from marine cyanobacteria using combined phylogenetic and mass spectrometric evaluation. *J.*
410 *Nat. Prod.* **78**, 486–492 (2015).
- 411 4. Ratnayake, R. *et al.* Dolastatin 15 from a Marine Cyanobacterium Suppresses HIF-1 α Mediated
412 Cancer Cell Viability and Vascularization. *ChemBioChem* (2020) doi:10.1002/cbic.202000180.
- 413 5. Bai, R., Pettit, G. R. & Hamel, E. Binding of dolastatin 10 to tubulin at a distinct site for peptide
414 antimitotic agents near the exchangeable nucleotide and vinca alkaloid sites. *J. Biol. Chem.* **265**,
415 17141–17149 (1990).

- 416 6. Cruz-Monserrate, Z., Mullaney, J. T., Harran, P. G., Pettit, G. R. & Hamel, E. Dolastatin 15 binds
417 in the vinca domain of tubulin as demonstrated by Hummel-Dreyer chromatography. *Eur. J.*
418 *Biochem.* **270**, 3822–3828 (2003).
- 419 7. Bousquet, M. S. *et al.* Multidimensional screening platform for simultaneously targeting
420 oncogenic KRAS and hypoxia-inducible factors pathways in colorectal cancer. *ACS Chem. Biol.*
421 **11**, 1322–1331 (2016).
- 422 8. Pouyssegur, J., Dayan, F., Mazure, N. M. Hypoxia signalling in cancer and approaches to enforce
423 tumour regressio. *Nature* **441**, 437–443 (2006).
- 424 9. Semenza, G. L. Targeting HIF-1 for cancer therapy. *Nat. Rev. Cancer* **3**, 721–732 (2003).
- 425 10. Zhong, H. *et al.* Overexpression of hypoxia-inducible factor 1 α in common human cancers and
426 their metastases. *Cancer Res.* **59**, 5830–5835 (1999).
- 427 11. Paul, V. J., Thacker, R. W., Banks, K. & Golubic, S. Benthic cyanobacterial bloom impacts the
428 reefs of South Florida (Broward County, USA). *Coral Reefs* **24**, 693–697 (2005).
- 429 12. Sharp, K. *et al.* Phylogenetic and chemical diversity of three chemotypes of bloom-forming
430 *Lyngbya* species (cyanobacteria: Oscillatoriales) from reefs of southeastern Florida. *Appl.*
431 *Environ. Microbiol.* **75**, 2879–2888 (2009).
- 432 13. Matthew, S. *et al.* Intramolecular modulation of serine protease inhibitor activity in a marine
433 cyanobacterium with antifeedant properties” *Mar. Drugs* **8**, 1803–1816 (2010).
- 434 14. Umezawa, K., Ikeda, Y., Kawase, O., Naganawa, H. & Kondo, S. Biosynthesis of polyoxypeptin
435 A: Novel amino acid 3-hydroxy-3- methylproline derived from isoleucine. *J. Chem. Soc. Perkin*
436 *Trans I* **13**, 1550–1553 (2001).
- 437 15. Steele, A. D. *et al.* Diverted total synthesis of promysalin analogs demonstrates that an iron-
438 binding motif is responsible for its narrow-spectrum antibacterial activity. *J. Am. Chem. Soc.* **138**,
439 5833–5836 (2016).
- 440 16. Luesch, H. *et al.* Biosynthesis of 4-methylproline in cyanobacteria: Cloning of nosE and nosF
441 genes and biochemical characterization of the encoded dehydrogenase and reductase activities. *J.*
442 *Org. Chem.* **68**, 83–91 (2003).
- 443 17. Mattingly, P. G. & Miller, M. J. Titanium trichloride reduction of substituted N-hydroxy-2-
444 azetidinones and other hydroxamic acids. *J. Org. Chem.* **45**, 410–415 (1980).
- 445 18. Kim, B. *et al.* Evaluation of class I HDAC isoform selectivity of largazole analogues. *Bioorganic*
446 *Med. Chem. Lett.* **24**, 3728–3731 (2014).
- 447 19. Ley, S. V., Prieur, A. & Heusser, C. Total synthesis of the cyclic heptapeptide Argyrin B: A new
448 potent inhibitor of T-cell independent antibody formation. *Org. Lett.* **4**, 711–714 (2002).
- 449 20. Sendai, M., Hashiguchi, S., Tomimoto, M., Kishimoto, S., Matsuo, T., Ochiai, M. Synthesis of
450 carumonam (AMA-1080) and a related compound starting from (2R,3R)-epoxysuccinic acid.
451 *Chem. Pharm. Bull* **33**, 3798–3810 (1985).
- 452 21. Guzman-Martinez, A., VanNieuwenhze, M. An operationally simple and efficient synthesis of
453 orthogonally protected L-threo-b-hydroxyasparagine. *Synlett* **10**, 1513–1516 (2007).
- 454 22. Boger, D. L., Lee, R. J., Bounaud, P. Y. & Meier, P. Asymmetric synthesis of orthogonally

- protected L-threo- β -hydroxyasparagine. *J. Org. Chem.* **65**, 6770–6772 (2000).
23. Shustov, G. V.; Chandler, M. K & Wolfe, S. Stereoselective synthesis of multiply substituted [1,2]oxazinan-3-ones via ring-closing metathesis. *Can. J. Chem.* **83**, 92–103 (2005).
24. Hale K. J., S. M. & George J. Total synthesis of (+)-A83586C, (+)-kettapeptin and (+)-azinothricin: powerful new inhibitors of β -catenin/TCF4- and E2F-mediated genetranscription. *Chem. Commun.* **46**, 4021–4042 (2010).
25. Hale, K. J., Manaviazar S., George J., Walters, M. A. & Dalby, S. M. Total synthesis of (+)-azinothricin and (+)-kettapeptin. *Org. Lett.* **11**, 733–736 (2009).
26. Ottenheijm, H. C. J. & Herscheid, J. D. M. N-Hydroxy- α -amino Acids in Organic Chemistry. *Chem. Rev.* **86**, 697–707 (1986).
27. Li, P. & Xu, J. C. 1-Ethyl 2-halopyridinium salts, highly efficient coupling reagents for hindered peptide synthesis both in solution and the solid-phase. *Tetrahedron* **56**, 8119–8131 (2000).
28. Smith, A. B. *et al.* Design, synthesis, and biological evaluation of EF- and ABEF- analogues of (+)-Spongistatin 1. *Org. Lett.* **12**, 1792–1795 (2010).
29. Shute, R. E. & Rich, D. H. Prevention of diketopiperazine formation in peptide synthesis by a simultaneous deprotection-coupling procedure: Entrapment of reactive nucleophilic species by in situ acylation. *J. Chem. Soc. Chem. Commun.* 1155–1156 (1987) doi:10.1039/C39870001155.
30. Kogen, H. *et al.* Crystal structure and total synthesis of globomycin: Establishment of relative and absolute configurations [5]. *J. Am. Chem. Soc.* **122**, 10214–10215 (2000).
31. Bajjuri, K. M., Liu, Y., Liu, C. & Sinha, S. C. The legumain protease-activated auristatin prodrugs suppress tumor growth and metastasis without toxicity. *ChemMedChem* **6**, 54–59 (2011).
32. Gaucher-Wieczorek, F. S., Maillard, L. T., Badet, B. & Durand, P. Fluorous tagged N-hydroxy phthalimide for the parallel synthesis of O-aryloxyamines. *J. Comb. Chem.* **12**, 655–658 (2010).
33. Schwartz, E. L. Antivascular actions of microtubule-binding drugs. *Clin. Cancer Res.* **15**, 2594–2601 (2009).
34. Paul K. D., Hamel E., M. L. *Cancer Chemotherapeutic Agents*. (American Chemical Society Books, Washington, DC, 1995).
35. Parker, A. L., Teo, W. S., McCarroll, J. A. & Kavallaris M. An emerging role for tubulin isotypes in modulating cancer biology and chemotherapy resistance. *Int. J. Mol. Sci.* **18**, 1434 (2017).
36. Doodhi, H. *et al.* Termination of protofilament elongation by eribulin induces lattice defects that promote microtubule catastrophes. *Curr. Biol.* **26**, 1713–1721 (2016).
37. Menchon, G. *et al.* A fluorescence anisotropy assay to discover and characterize ligands targeting the maytansine site of tubulin. *Nat. Commun.* **9**, 1–9 (2018).
38. La Regina, G. *et al.* Arylthioindole inhibitors of tubulin polymerization. 3. Biological evaluation, structure-activity relationships and molecular modeling studies. *J. Med. Chem.* **50**, 2865–2874 (2007).

39. Diaz, J. F. & Andreu, J. M. Kinetics of dissociation of the tubulin-colchicine complex. Complete reaction scheme and comparison to thermodynamic measurements, *J. Biol. Chem.* **266**, 2890-2896 (1991).
40. Risinger, A. L. *et al.* The taccalonolides: Microtubule stabilizers that circumvent clinically relevant taxane resistance mechanisms. *Cancer Res.* **68**, 8881–8888 (2008).
41. Čermák, V. *et al.* Microtubule-targeting agents and their impact on cancer treatment. *Eur. J. Cell Biol.* **99**, 151075, (2020).
42. Prota, A. E. *et al.* Structural basis of tubulin tyrosination by tubulin tyrosine ligase. *J. Cell Biol.* **200**, 259–270 (2013).
43. Weinert, T. *et al.* Serial millisecond crystallography for routine room-temperature structure determination at synchrotrons. *Nat. Commun.* **8**, (2017).
44. Luesch, H. & MacMillan, J. B. Targeting and extending the eukaryotic druggable genome with natural products. *Nat. Prod. Rep.* **37**, 744–746 (2020).
45. Matthew, S., Ross, C., Paul, V. J. & Luesch, H. Pompanopeptins A and B, new cyclic peptides from the marine cyanobacterium *Lyngbya confervoides*. *Tetrahedron* **64**, 4081–4089 (2008).
46. Matthew, S., Paul, V. J. & Luesch, H. Tiglicamides A-C, cyclodepsipeptides from the marine cyanobacterium *Lyngbya confervoides*. *Phytochemistry* **70**, 2058–2063 (2009).
47. Matthew, S., Paul, V. J. & Luesch, H. Largamides A - C, tiglic acid-containing cyclodepsipeptides with elastase-inhibitory activity from the marine cyanobacterium *Lyngbya confervoides*. *Planta Med.* **75**, 528–533 (2009).
48. Tan, L. T. & Phyto, M. Y. Marine cyanobacteria: A source of lead compounds and their clinically-relevant molecular targets. *Molecules*, **25**, 2197 (2020).
49. Bertrand, S., Hélesbeux, J.-J., Larcher G. & Duval, O. Hydroxamate, a key pharmacophore exhibiting a wide range of biological activities. *Mini Rev Med Chem* **13**, 1311–1326 (2013).
50. Prota, A. E. *et al.* A new tubulin-binding site and pharmacophore for microtubule-destabilizing anticancer drugs. *Proc. Natl. Acad. Sci. U. S. A.* **111**, 13817–13821 (2014).
51. Prota, A. E. *et al.* Pironetin Binds Covalently to α Cys316 and Perturbs a Major Loop and Helix of α -Tubulin to Inhibit Microtubule Formation. *J. Mol. Biol.* **428**, 2981–2988 (2016).
52. Ravelli, R. B. G. *et al.* Insight into tubulin regulation from a complex with colchicine and a stathmin-like domain. *Nature* **428**, 198–202 (2004).
53. Gigant, B. *et al.* Structural basis for the regulation of tubulin by vinblastine. *Nature* **435**, 519–522 (2005).
54. Oliva, M. A. *et al.* Structural Basis of Noscapine Activation for Tubulin Binding. *J. Med. Chem.* **63**, 8495–8501 (2020).
55. Wang, Y. *et al.* Structures of a diverse set of colchicine binding site inhibitors in complex with tubulin provide a rationale for drug discovery. *FEBS J.* **283**, 102–111 (2016).

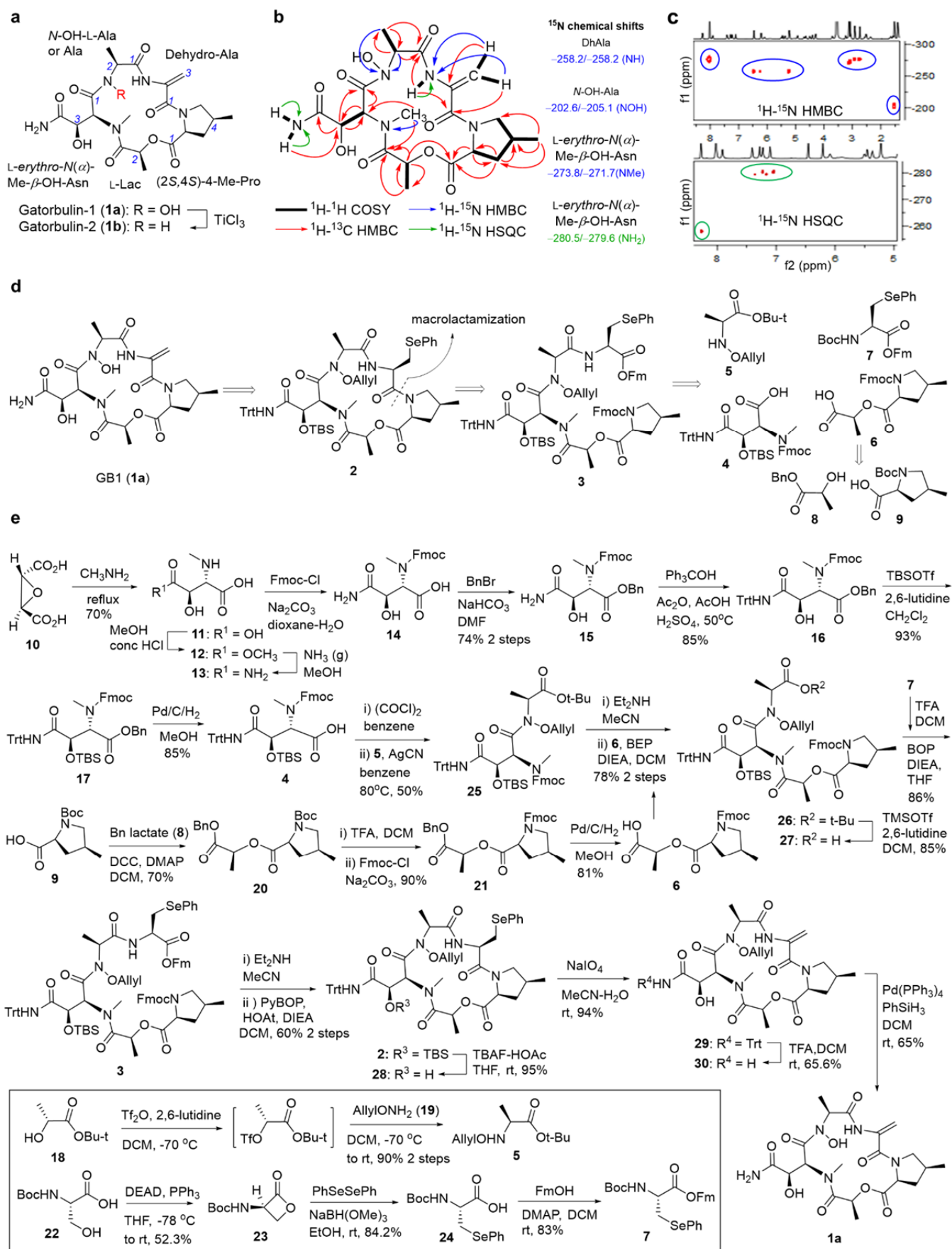
530

531 **Figures**

532

533 **Figure 1. Binding sites and structures of microtubule-targeting agents.** **a**, Tubulin heterodimer (β -
 534 tubulin grey and α -tubulin white) in ribbon representation, where six known binding sites have been
 535 highlighted showing representative ligands in sphere representation: maytansine (PDB 4tv8, violet);
 536 epothilone (PDB 4o4i, orange); peloruside (PDB 4o4j, red); colchicine (PDB 4o2b, dark blue); pironetin

537 (PDB 5fny, cyan) and, vinblastine (PDB 4eb6, light blue). New gatorbulin binding site has been also
538 included (PDB 7alr, teal). **b,c** Representative compounds targeting tubulin binding sites. **b**, Microtubule-
539 stabilizing agents. **c**, Microtubule-destabilizing agents, including the structure of gatorbulin-1 (**1a**).



541 **Figure 2. Structure determination and total synthesis of gatorbulin-1** **a**, Structures of the isolated
542 natural products, gatorbulin-1 (GB1, **1a**) and its *N*-deoxy-derivative, gatorbulin-2 (GB2, **1b**). **b**, Homo-
543 and heteronuclear 2D NMR correlations for GB1. **c**, Selected regions of the ^1H - ^{15}N HMBC and ^1H - ^{15}N
544 HSQC spectra of GB1. **d**, Retrosynthetic analysis of the total synthesis of gatorbulin-1 (GB1, **1a**). **e**,
545 Forward synthetic route.

546

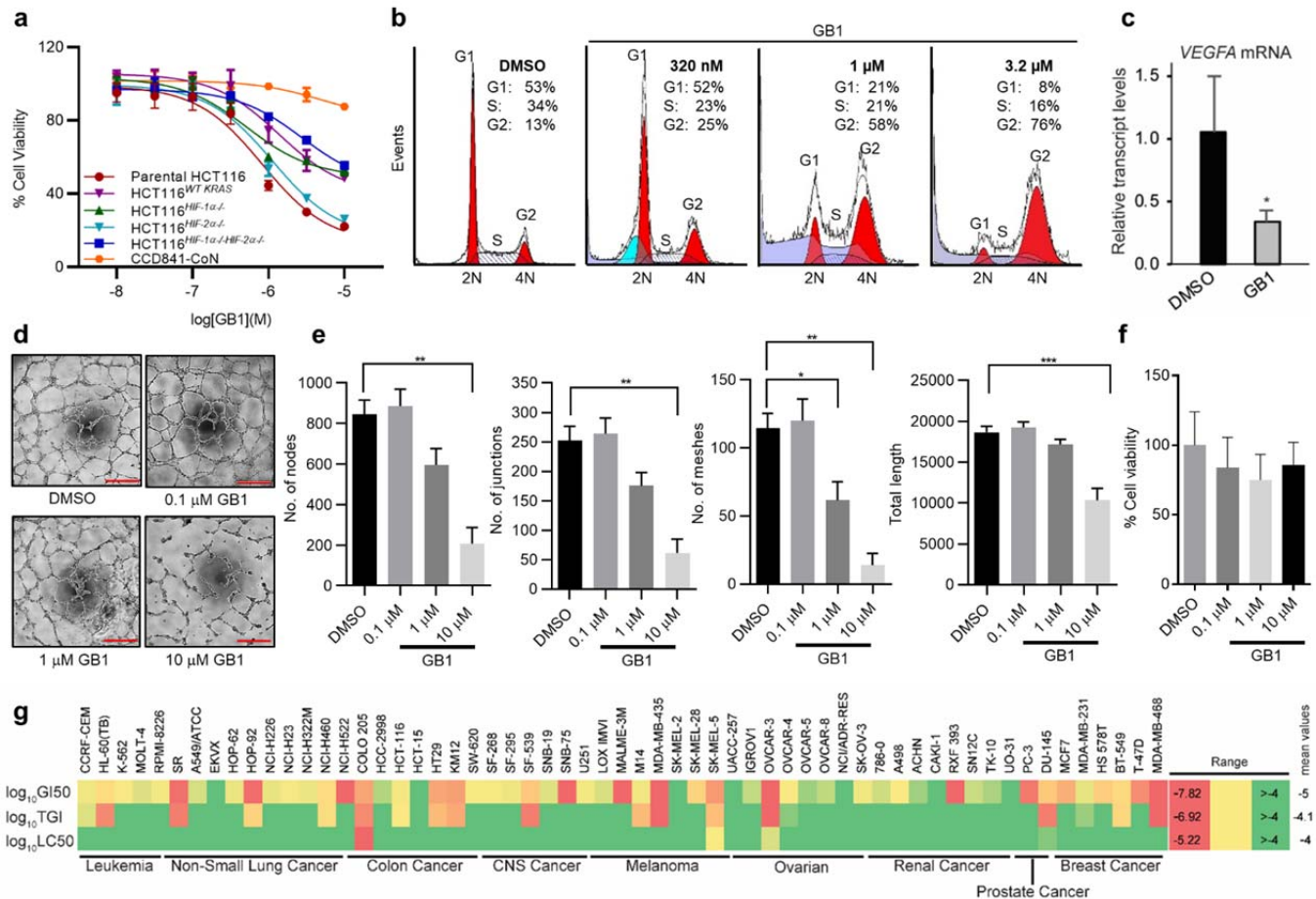


Figure 3. Mechanism of action of gatorbulin-1 through cellular profiling. **a**, Antiproliferative activity of GB1 in parental HCT116 colon cells, isogenic HCT116 knockout cells, and CCD-841CoN normal epithelial colon cells (48 h treatment). GB1 showed a marginal effect on the viability of CCD-841CoN normal epithelial colon cells. Parental HCT116 cells and HCT116^{HIF-2α} were most susceptible, while the potency and efficacy of GB1 was reduced against HCT116^{HIF-1α/-HIF-2α/-}, HCT116^{HIF-1α/-}, and oncogenic KRAS knockout (HCT116^{WT KRAS}). Cell viability was measured by MTT assay. **b**, Cell cycle analysis. HCT116 cells were treated with GB1 for 24 h (320 nM, 1 μM, 3.2 μM) and DNA content assessed by flow cytometry of propidium iodide stained cells. GB1 induced G2/M accumulation. **c**, HIF target gene (*VEGFA*) expression after 16 h exposure of parental HCT116 cells to GB1 (3.2 μM). RNA was isolated, reverse transcribed and subjected to qPCR using TaqMan analysis. *β-actin* served as endogenous control. Error bars indicate mean ± SD of three replicates (student *t* test, **p* < 0.05). **d,e,f**, GB1 inhibits HUVEC tube formation *in vitro* without toxicity. **d**, Representative images of HUVEC tube formation in growth factor-reduced Matrigel upon treatment with DMSO or varying concentrations (10 μM, 1 μM or 0.1 μM) of GB1 (9 h). Scale bar: 200 μm. All images shown are representative and data are represented as mean ± SEM; One-way ANOVA followed by Tukey's multiple comparisons test; **p* < 0.05, ***p* < 0.01 and ****p* < 0.001. **e**, Quantification of number of nodes, number of junctions, number of meshes and total length of tubes (n = 3). **f**, GB1 does not affect HUVEC cell viability. HUVEC cell viability was quantified by absorbance at 490 nm using MTS assay (24 h). GB1 treatment did not affect total number of viable HUVEC cells compared to DMSO-treated control (n=3). For panels **e** and **f**, data are represented as mean ± SEM; One-way ANOVA followed by Tukey's multiple comparisons test. **g**, Heatmap for the performance of GB1 across cell lines in the NCI-60 screen using

569 three different values (growth-inhibitory effect, GI_{50} ; cytostatic effect, TGI; cytotoxic effect, LC_{50} ;
570 concentration in M).
571

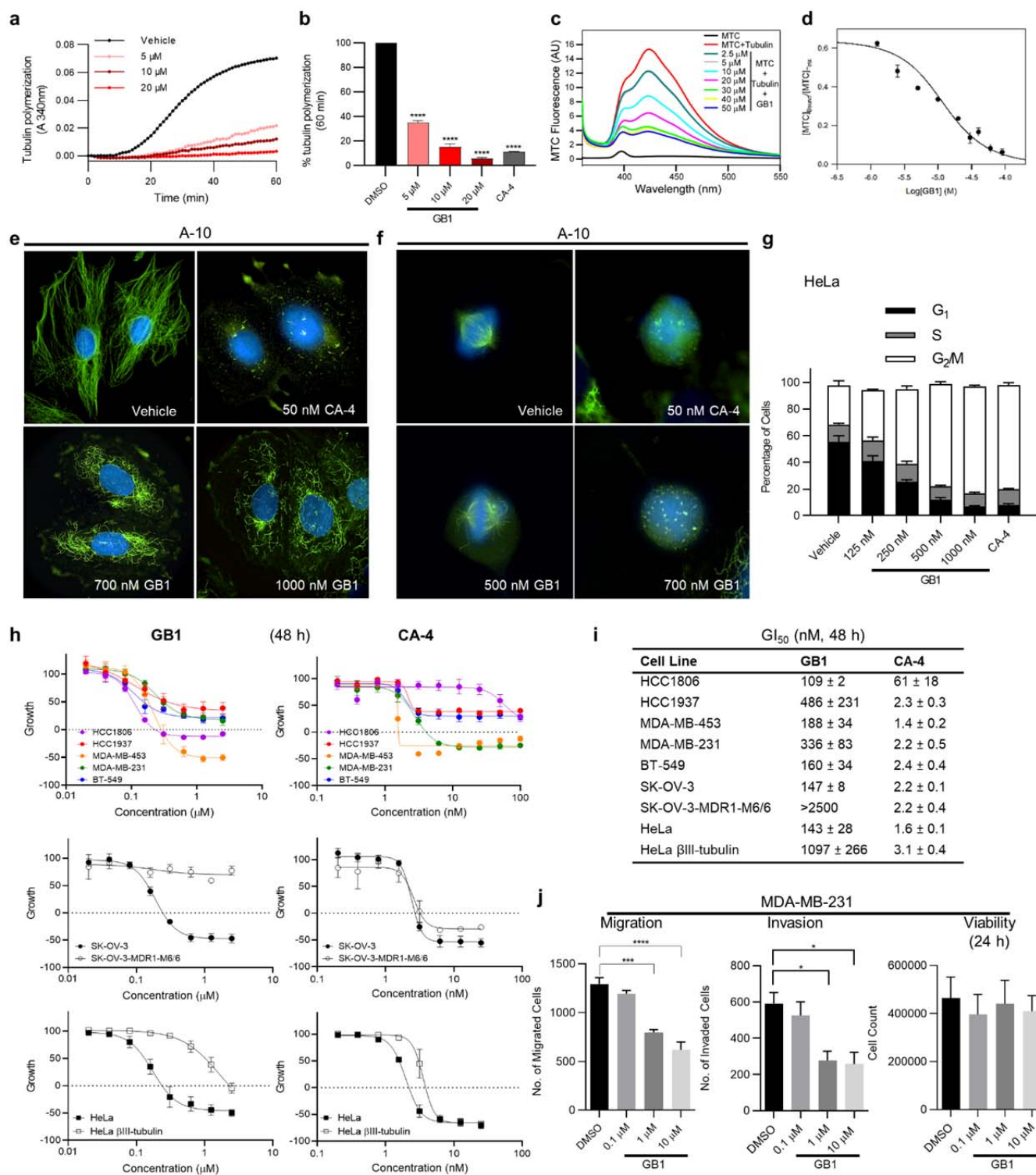


Figure 4. Target identification and selectivity profiling of GB1 in comparison with colchicine binder combretastatin A-4 (CA-4) in different cell types and resistance models. a,b, GB1 directly inhibits the polymerization of purified tubulin. **a**, Polymerization of purified porcine brain tubulin (20 μM) over time as monitored by light scattering at 340 nm with vehicle (DMSO) or 5–20 μM GB1. **b**, Quantification of tubulin polymerization at 60 min. Error bars represent ± SEM from two independent experiments. One-way ANOVA with Dunnett's post-hoc test, **** $p < 0.0001$. **c,d**, Displacement of 2-methoxy-5-(2,3,4-trimethoxyphenyl)-2,4,6-cycloheptatrien-1-one (MTC) from the colchicine site. **c**,

580 Fluorescence emission spectra of 10 μ M MTC in 10 mM phosphate-0.1 mM GTP buffer pH 7.0 in the
 581 absence (black line) and the presence of 10 μ M tubulin (red line) plus varying concentrations (5–50 μ M)
 582 of GB1. **d**, Displacement isotherm at 25 °C of MTC by GB1. The data points were fit to the best value
 583 of the binding equilibrium constant of GB1, assuming 0.8 sites per tubulin dimer. **e**, GB1 promotes
 584 microtubule depolymerization in interphase cells. **e**, A-10 cells were treated with vehicle (DMSO), 50
 585 nM CA-4, 700 nM GB1, or 1000 nM GB1 for 18 h. Microtubules were visualized using a β -tubulin
 586 antibody (green) and DNA was visualized using DAPI (blue). Images are representative of three
 587 independent experiments. **f**, GB1 promotes formation of aberrant mitotic spindles. A-10 cells were
 588 treated with vehicle (DMSO), 25 nM CA-4, 500 nM GB1, or 700 nM GB1 for 18 h. Mitotic spindles
 589 were visualized using a β -tubulin antibody (green) and DNA with DAPI staining (blue). Images are
 590 representative of three independent experiments. **g**, GB1 promotes concentration-dependent
 591 accumulation of cells in the G₂/M phases of the cell cycle in HeLa cells. HeLa cells were treated with
 592 vehicle (DMSO), 125–1000 nM GB1, or 100 nM CA-4. Cell cycle distribution was evaluated by
 593 quantification of propidium iodide staining by flow cytometry. Error bars represent \pm SEM from three
 594 independent experiments. **h,i**, Antiproliferative and cytotoxic effects of GB1 and CA-4 in a panel of
 595 TNBC cell lines, in parental and Pgp- expressing SK-OV-3 cells, or in parental and β III expressing
 596 HeLa cells (sulforhodamine B assay). **h**, Dashed line at y = 0 denotes cell density at the time of
 597 compound addition with negative y-values indicating cytotoxicity. **i**, Concentrations that caused a 50%
 598 decrease in growth inhibition (GI₅₀) were determined by non-linear regression. Results represent three
 599 independent experiments \pm SEM. **j**, Effects of GB1 on transwell migration and invasion of MDA-MB-
 600 231 breast cancer cells pre-treated with GB1 for 24 h. Pre-treated cells were allowed to migrate or
 601 invade for 5 h, and both processes were inhibited in a dose-dependent manner. Quantitative analysis of
 602 migrated or invaded DMSO or GB1 pre-treated MDA-MB-231 cells across a matrigel layer (n=3). GB1
 603 treatment does not affect overall MDA-MB-231 cancer cell count (24 h) as determined by Trypan Blue
 604 exclusion assay (n=3). Data are represented as mean \pm SEM; One-way ANOVA followed by Tukey's
 605 multiple comparisons test; *p < 0.05, ***p < 0.001.

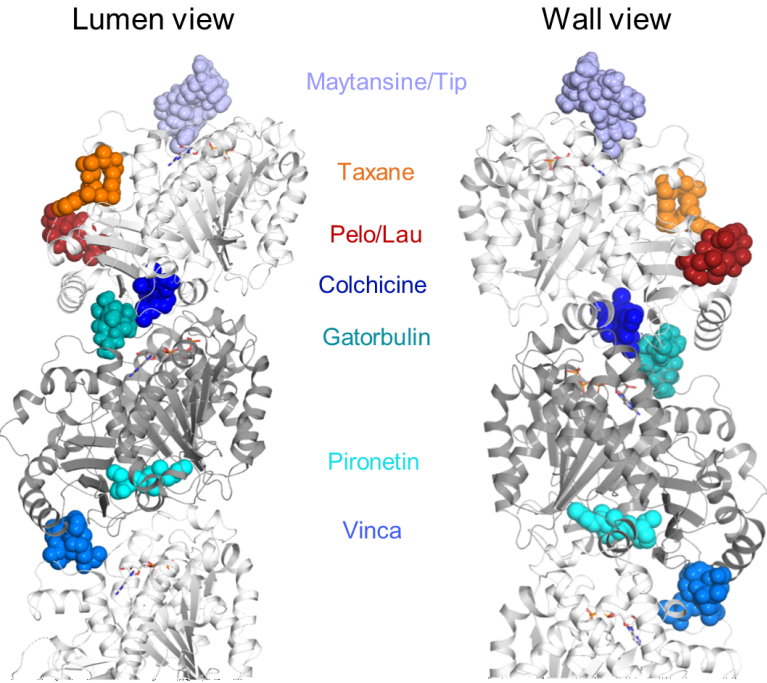
607 **Figure 5. Crystal structure of TD1-gatorbulin-1 complex.** **a**, Overall view of the TD1-GB1 complex
608 (PDB 7alr). Tubulin (α -tubulin grey and β -tubulin light grey) and DarPin (green) are in ribbon, and
609 tubulin bound nucleotides (orange) and the ligand GB1 (teal) are in sphere representation, respectively.
610 **b**, Zoom into the composite Gatorbulin-1 site. Simulated annealing omit map of GB1 in the
611 corresponding TD1 complex structure. The mFo-DFc electron density map (grey mesh) is contoured at
612 3.0σ . The GB1 molecule is shown in stick representation and α - and β -tubulin in ribbon labeling the
613 secondary structural elements involve in protein-compound interaction in blue. **c,d**, Close-up view of the
614 interaction observed between GB1 (teal, sticks) and tubulin (α -tubulin grey and β -tubulin light grey,
615 ribbon). Interacting residues are shown in stick representation and are labeled. Panel **d** is a rotated view
616 of panel **c**. **e**, Comparison of GB1 (teal) and colchicine (blue) binding sites, where tubulin in ribbon and
617 ligands in stick representation. Zoom in panels to show α -tubulin loop T5 and β -tubulin loop T7
618 conformational changes required for colchicine accommodation when compared colchicine (PDB 5nm5)
619 and GB1 (PDB 7alr) structures. Ligands in stick representation (GB1, teal and, colchicine, blue) and
620 tubulin in ribbon representation (PDB 5nm5, blue and, PDB 7alr, grey). Main residues involved are in
621 stick representation and labeled.

622 **Table 1.** NMR data for gatorbulin-1 (GB1, **1a**) for both conformers (1:1) in DMF-*d*₇
623

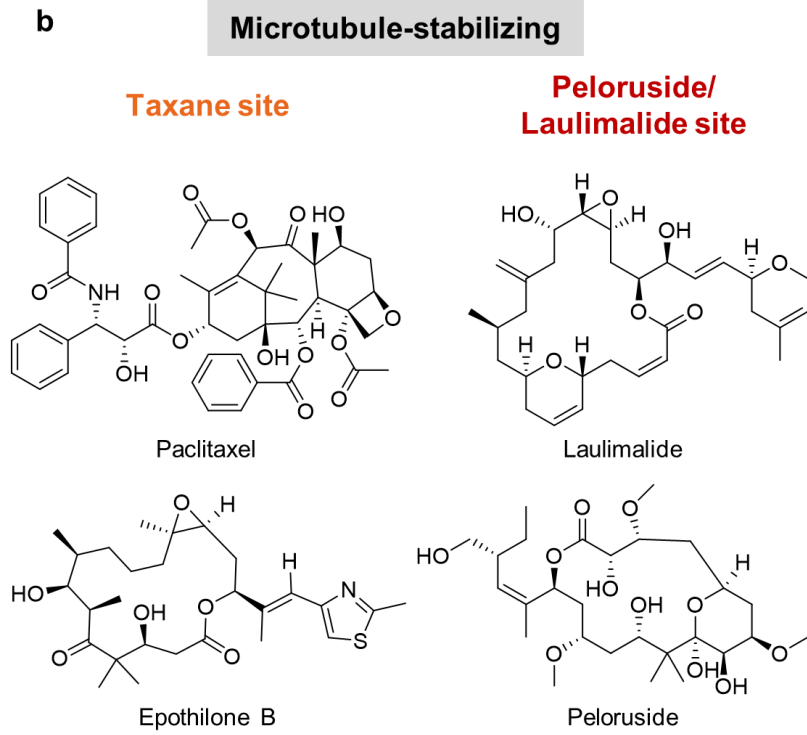
unit	C/H no.	conformer 1					conformer 2			
		δ_{H} (J in Hz) ^a	δ_{C} , mult ^b	δ_{N} ^c	COSY ^a	¹ H- ¹³ C HMBC ^a	¹ H- ¹⁵ N HMBC ^d	δ_{H} (J in Hz) ^a	δ_{C} , mult ^b	δ_{N} ^c
DhAla	1		165.9, qC						166.8, qC	
	2		136.3, qC						136.2, qC	
	3a	6.46, s	101.8, CH ₂		H-3b	1, 2		6.22, s	103.0, CH ₂	
	3b	5.22, s			H-3 ^a	1		5.11, s		
	NH	8.28, s		-258.2		1, 1 (Ala)	H-3a, H-3b	8.60, s		-258.2
N-OH-Ala	1		170.5, qC						170.2, qC	
	2	4.29, q (6)	64.7, CH		H ₃ -3, NH	1, 3		4.71, br q (6)	60.0, CH	
	3	1.54, d (6)	13.8, CH ₃		H-2	1, 2		1.42, d (6)	15.6, CH ₃	
	N-OH	11.35, br s		-202.6			H-2, H ₃ -3	10.58, br		-205.1
N(α)-Me- β -OH-Asn	1		170.4, qC						169.4, qC	
	2	5.51, br d (9.5)	58.0 (br), CH		H-3,	1, 2		5.85	not observed	
	3	4.51, dd (9.5, 4.5)	68.8, CH		H-2, 3-OH	1, 2, 4		4.65, br dd (6, 6)	69.7, CH	
	3-OH	6.05, br d			H-3			5.06, br		
	4		175.1, qC						174.8	
	N-Me	3.09, s	34.0, CH ₃	-273.8		2, 1 (Lac)	N-Me	3.14, s	34.5 (br), CH ₃	-271.7
	4-NHa	7.26, s		-280.5	4-NHb			7.39, s		-279.6
	4-NHb	7.09, s			4-NHa	3		7.21, s		
Lac	1		169.9, qC						169.7, qC	
	2	5.47, q (7.0)	72.9, CH		H ₃ -3	1, 3, 1 (MePro)		5.39, q (7.0)	72.1, CH	
	3	1.42, d (7.0)	17.6, CH ₃		H-2	1, 2		1.41, d (7.0)	17.3, CH ₃	
4-Me-Pro	1		170.8, qC						170.4, qC	
	2	4.42, t (7.0)	62.6, CH		H-3a, H-3b	1, 3		4.94, dd (9, 8)	63.8, CH	
	3a (<i>proS</i>)	2.58, m	37.0, CH ₂		H-2, H-3b, H-4	1, 2, 4, 5, 6		2.53, m	40.8, CH ₂	
	3b (<i>proR</i>)	1.58, m			H-2, H-3a, H-4	1, 2, 4, 5, 6		1.65, m		
	4	2.53, m	34.7, CH		H-3a, H-3b, H-5a, H-5b, H ₃ -6	3, 5, 6		2.38, m	32.4, CH	
	5a (<i>proR</i>)	4.31, dd (-10.0, 6.0)	56.9, CH ₂		H-4, H-5b	2, 3, 4, 6		3.71, dd (-11.0, 7.0)	55.6, CH ₂	
	5b (<i>proS</i>)	3.25, dd (-10.0, 8.5)			H-4, H-5a	3, 6		3.11, dd (-11.0, 11)		
	6	1.12, d (7.0)	18.0, CH ₃		H-4	3, 4, 5		1.11, d (7.0)	16.9, CH ₃	

^aRecorded at 600 MHz. ^bRecorded at 150 MHz. ^cDeduced from ¹H-¹⁵N HSQC and ¹H-¹⁵N HMBC (500 MHz). ^dRecorded at 500 MHz.

a



b



c

